Received: 27 September 2018 | Revised: 21 July 2019 | Accepted: 8 August 2019
DOI: 10.1002/navi.336

ORIGINAL ARTICLE

Angular accelerometer-based inertial navigation system

Uriel Nusbaum[1] | **Ilan Rusnak**[2] | **Itzik Klein**[3]

[1]Technion Autonomous Systems Program, Haifa, Israel
[2]Rafael Advanced Defense Systems Ltd, Haifa, Israel
[3]Department of Marine Technologies, University of Haifa, Israel

Correspondence
Uriel Nusbaum, Technion Autonomous Systems Program, Haifa, 3200003, Israel.
Email: urieln@campus.technion.ac.il

Abstract

Angular acceleration sensors technologies are evolving and emerging in various applications. In this paper, we propose an angular accelerometer-based inertial navigation system. One application of such systems can be highly maneuvering platforms where direct measurement of angular acceleration is desired. To that end, a review of modern angular acceleration sensor technologies and their possible applications is provided. Two angular acceleration-based inertial navigation system architectures are suggested, and their equations of motion are derived. Additionally, an analytical assessment for short time periods of pure inertial navigation is provided with a comparison to traditional and gyro-free inertial navigation architectures.

1 | INTRODUCTION

Generally, an inertial navigation system (INS) has two main components: inertial sensors and a navigation computer. The inertial sensors are accelerometers and gyroscopes and together they form an inertial measurement unit (IMU). The IMU produces measurements of the specific force and angular velocity of its carrying platform. These measurements are then processed in the navigation computer to yield an estimate of the platform position, velocity, and orientation. Traditional IMU architecture includes three orthogonal accelerometers and three orthogonal gyroscopes. Such architectures have been widely used since the 1960s[1] first for military and soon after for civilian usages. INS as well as its IMU and related fields theory are well studied in the literature and can be found in some excellent textbooks such as Broxmeyer, Titterton and Weston, Groves, Farrell[1-4] and more.

Nowadays, inertial technology is fundamental in smart and autonomous devices ranging from autonomous cars[5] through remote-operated robots[6] to augmented reality devices[7-9] and modern localization systems.[10] In addition, advantages of using inertial sensor arrays fusion has been recently introduced.[11] While navigation algorithms as well as new sensing technologies have been a major interest for research,[12,13] IMU architecture received little attention. Even though major breakthroughs in sensing, eg, MEMS-based IMU, allowed the development of low-cost INS, new applications that require inertial measurements that standard IMU cannot provide are emerging.

The use of angular acceleration in inertial navigation systems was considered in the past.[2,14] However, the idea was quickly abandoned mainly due to technology issues the sensors had in that time. Yet, as for today, there are many breakthroughs in angular accelerometer technology, and we believe this direction will continue enabling the usage of angular accelerometers in other applications in a similar way that Micro-Electro Mechanical Systems (MEMS) technology opened a new era with new applications for linear accelerometers and gyroscopes (eg, smartphone or shoe-based navigation).

Today, all INSs are based on the traditional IMU architecture, yet another type of architecture known as gyro-free INS (GFINS) or all accelerometer INS exists. The development of GFINS is mainly motivated by some inherent properties of gyroscopes. First, gyroscopes are more energy consuming than accelerometers. Second, they are relatively expensive and third, advances in MEMS accelerometers make them perform better at lower price ranges. When combining these factors with the infiltration of INS to consumer-level mobile products, such as smartphones and virtual reality gear, the ever-growing need of developing cheaper systems without performance sacrifice is obvious. In GFINS, a set of $N \geq 6$

accelerometers are attached to the navigating platform and replaced the conventional use of gyroscopes.[15] Different sensor positioning options are available, which allow installation flexibility and performance enhancements.[11] An important feature of GFINS is its ability to measure angular acceleration that enables it to perform both as standard INS and as a measuring device when angular acceleration measurement is needed.[16] However, GFINS suffers from various errors caused by inaccurate accelerometer positioning that in turn affects both estimation accuracy and signal to noise ratio (SNR).

Since accelerometer positioning affects the GFINS performance, geometric configurations and their optimization has been a major interest for research.[17,18] In addition, the number of accelerometers in the sensors array is also a contributing factor to the overall performance, complexity, and cost. As such, this has also been at the center of focus for the research community.[19] Recent studies of systems theory properties of GFINS have also been published.[20,21]

In parallel to the major development of linear accelerometers and gyroscopes, angular accelerometer technologies have emerged.[22,23] Measuring angular acceleration has numerous applications ranging from vehicle ride experience enhancement[24] and safety mechanisms,[25,26] through flight control systems and ejection seat testing for the aerospace industry, as well as traditional industry applications, eg, turbine health monitoring, industrial robot control systems, and more.

When control actions produce torques, it is beneficial to use angular acceleration feedback as a means for realization of full-state feedback. This issue was raised in Devasia, Eleftheriou, and Moheimani,[27] where realization of nano positioning systems for atomic force microscopes, scanning probe microscopes, and hard disk drive servo systems is discussed. Most of the literature on angular acceleration measurements reviewed the effects of direct measurement of angular acceleration and compared it to indirect inference of it[22] mostly focusing on noise and delay influences.

In this paper, we propose using angular accelerometer sensors as an alternative or in addition to gyroscopes in traditional inertial navigation system (TINS) architectures. We suggest two angular accelerometer-based INS configurations:

1. Angular accelerometer INS (AINS). In this configuration, the angular accelerometers replace the gyroscopes entirely. Three orthogonal angular accelerometers and three orthogonal linear accelerometers are needed.
2. Angular accelerometer aided INS (AAINS). In AAINS, angular accelerometers are added in addition to the use of gyroscopes thus aiding the measurements. This configuration requires three orthogonal linear accelerometers, three orthogonal angular accelerometers, and three orthogonal gyroscopes.

Since angular acceleration is measured directly in both configurations, it is expected that the angular accelerometer-based INS will be valuable for highly maneuverable platforms where angular acceleration changes rapidly, eg, skidding vehicles, racing drones, launch vehicles, and vibrating platforms. There, angular accelerometers will enhance tracking abilities compared to TINS or GFINS, which do not measure angular acceleration directly. In such maneuvering platforms, angular accelerometers will offer direct measurement of angular acceleration thus allowing better orientation estimation. On the other hand, in pure inertial navigation, the sensor errors will accumulate more rapidly compared to traditional INS architecture since the angular acceleration must be integrated to obtain the angular velocity as required in the traditional INS equations of motion. Therefore, accelerometer-based INS, with current available technology, is capable of pure inertial navigation for very short time periods. It is for this reason that external updates such as GNSS will be required.

The structure the paper is as follows. Section 2 provides the necessary background and equations of motion for TINS and GFINS. Section 3 discusses the operational principles of angular accelerometer technology and provides a literature review. Section 4 presents two angular accelerometer-based INS configurations while in Section 5, the analytical assessment of the AINS is provided for short-term navigation. Conclusions are given in Section 6.

2 | INS CONFIGURATIONS

Generally speaking, TINS consists of two main components. The first is a navigation computer that solves the navigation equations and outputs an estimate of the carrying platform state (six DOF positions and velocities). The second component is an inertial measurement unit (IMU)—a sensor suite that can measure physical quantities related to the platform state, eg, specific force, angular velocity/acceleration, etc.

2.1 | Traditional INS

TINS is composed of three orthogonal accelerometers for specific force measurement and three orthogonal gyroscopes for angular velocity measurement. A simplified block diagram of TINS is presented in Figure 1. TINS equations are usually expressed in the navigation coordinates frame and consist of the following states:

1. p_{LLH}, position vector (latitude ϕ, longitude λ, and height h).
2. v_{eb}^{n}, velocity vector expressed in the navigation frame (v_n north, v_e east, and v_d down).
3. T_b^n, transformation matrix, body to navigation frame.

$$\begin{aligned} \dot{p}_{LLH} &= \left[\frac{v_n}{R_M+h} + \frac{v_d}{(R_N+h)\cos\phi} - v_d\right]^T \\ \dot{v}_{eb}^{n} &= \dot{T}_b^{n} f_{ib}^{b} + g_{ib}^{n} - \left(\Omega_{en}^{n} + 2\Omega_{ie}^{n}\right)v_{eb}^{n} \\ \dot{T}_b^{n} &= T_b^n\Omega_{ib}^{b} - \left(\Omega_{ie}^{n} + \Omega_{en}^{n}\right)T_b^n \end{aligned}, \tag{1}$$

where R_M is the meridian local radius of curvature, R_N is the normal local radius of curvature, Ω_{ie}^n is the skew symmetric form of the Earth rate vector expressed in the navigation frame, and Ω_{en}^n is the skew symmetric form of the navigation frame rate vector relative to the Earth-centered Earth-fixed (ECEF) frame expressed in the navigation frame. g_{ib}^n is the gravity vector, expressed in the navigation frame. The inputs to (1) are f_{ib}^b and ω_{ib}^b, which are the specific force acting on the body and angular velocities of the body, respectively (both expressed in the body frame). While TINS inputs contain direct measurements of the specific force and angular velocity, GFINS derives these quantities indirectly.

2.2 | Gyro-free INS

In GFINS, N ($N \geq 6$) accelerometers are arranged in a predetermined configuration around the platform center of mass. Using this configuration, the specific force and angular acceleration vectors can be derived and therefore position, velocity, and attitude can be calculated as illustrated in Figure 1. Each accelerometer yields the following output:

$$f_k^b = \left[e_k^b\right]^T\left\{f_i^b + \Omega_{ib}^b\Omega_{ib}^b\left[\rho_k^b\times\right]\dot{\omega}_{ib}^b\right\}, \tag{2}$$

where the subscript k refers to the k_{th} accelerometer and $\left[\rho_k^b\times\right]$ marks the skew symmetric form of the vector ρ_k^b, used to replace a cross product with its corresponding matrix multiplication. ρ_k^b is the position vector of the accelerometer with respect to the platform center of mass, and e_k^b is its sensitivity axis. Placing $N \geq 6$ accelerometers on predetermined locations yields the following equation:

$$\underbrace{\begin{bmatrix} f_1^b \\ \vdots \\ f_k^b \\ \vdots \\ f_N^b \end{bmatrix}}_{Y_{N\times 1}} = \underbrace{\begin{bmatrix} \left[\rho_1^b\times e_1^b\right]^T & \left[e_1^b\right]^T \\ \vdots & \vdots \\ \left[\rho_k^b\times e_k^b\right]^T & \left[e_k^b\right]^T \\ \vdots & \vdots \\ \left[\rho_N^b\times e_N^b\right]^T & \left[e_N^b\right]^T \end{bmatrix}}_{H_{N\times 6}} \begin{bmatrix} \dot{\omega}_{ib}^b \\ f_i^b \end{bmatrix} + \underbrace{\begin{bmatrix} \left[e_1^b\right]^T\Omega_{1b}^b\Omega_{1b}^b \\ \vdots \\ \left[e_k^b\right]^T\Omega_{kb}^b\Omega_{kb}^b \\ \vdots \\ \left[e_N^b\right]^T\Omega_{Nb}^b\Omega_{Nb}^b \end{bmatrix}}_{M_{N\times 1}}, \tag{3}$$

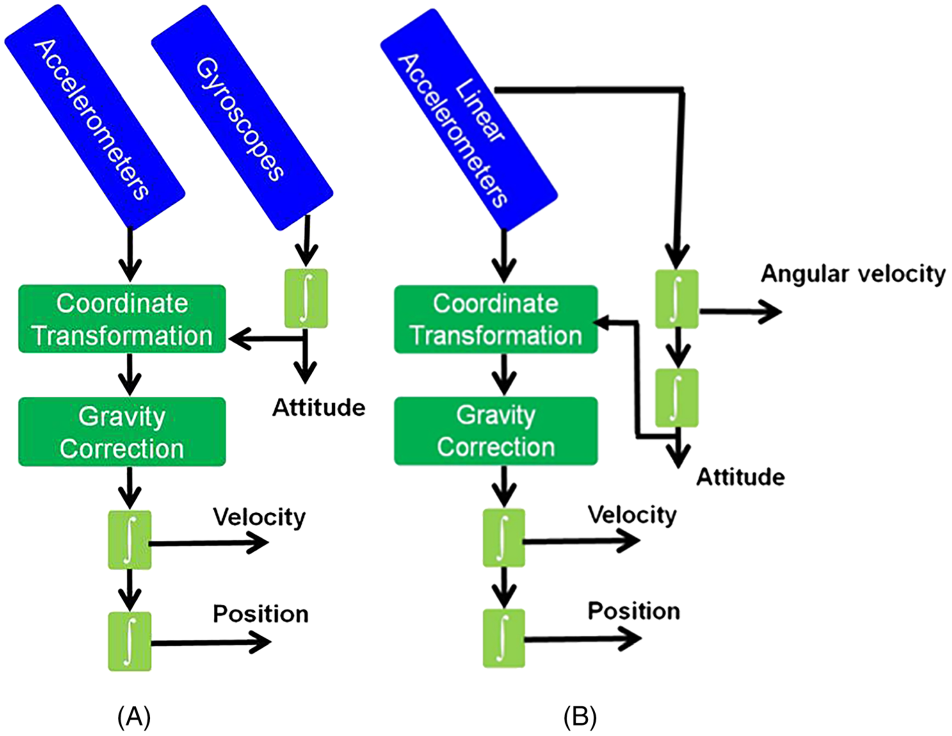

FIGURE 1 A simple block diagram to illustrate: (left) three accelerometers and three gyroscopes form a traditional INS architecture and (right) N accelerometers form a GFINS architecture [Color figure can be viewed at wileyonlinelibrary.com and www.ion.org]

and the measurement equation is derived by solving

$$\begin{bmatrix} \dot{\omega}_{ib}^{b} \\ f_{i}^{b} \end{bmatrix} = H^{\dagger}Y - H^{\dagger}M, \tag{4}$$

where Y is the measured specific force vector and $H^{\dagger}$ is the Moore-Penrose pseudo inverse of the configuration matrix H. For convenience, we divide $H^{\dagger}$ into two parts and write it as

$$H^{\dagger} = \begin{bmatrix} H_{\dot{\omega}}^{\dagger} \\ H_{f}^{\dagger} \end{bmatrix}. \tag{5}$$

The angular acceleration and specific force vectors are recovered separately as

$$\begin{matrix} \dot{\omega}_{ib}^{b} \\ f_{i}^{b} \end{matrix} = \begin{matrix} H_{\dot{\omega}}^{\dagger}Y - H_{\dot{\omega}}^{\dagger}M \\ H_{f}^{\dagger}Y - H_{f}^{\dagger}M \end{matrix}. \tag{6}$$

Finally, to formulate the GFINS equations of motion, we add ω_{ib}^{b} as an additional state to the INS, and the resultant equations are

$$\begin{aligned} \dot{p}_{LLH} &= \left[\frac{v_n}{R_M + h} + \frac{v_d}{(R_N + h)\cos\phi} - v_d\right]^{T} \\ \dot{v}_{eb}^{n} &= \dot{T}_{b}^{n}\left[H_{f}^{\dagger}Y - H_{f}^{\dagger}M\right] + g_{ib}^{n} - \left(\Omega_{en}^{n} + 2\Omega_{ie}^{n}\right)v_{eb}^{n}. \\ \dot{T}_{b}^{n} &= T_{b}^{n}\Omega_{ib}^{b} - \left(\Omega_{ie}^{n} + \Omega_{en}^{n}\right)T_{b}^{n} \\ \dot{\omega}_{ib}^{b} &= H_{\dot{\omega}}^{\dagger}Y - H_{\dot{\omega}}^{\dagger}M \end{aligned} \tag{7}$$

The input to (7) is the specific force vector Y. Note that a GFINS uses angular acceleration as a measurement even though it is not directly measured but derived.

3 | ANGULAR ACCELERATION TECHNOLOGIES

Before addressing the technologies used for sensing angular acceleration, we illustrate through a simple intuitive example how angular acceleration can be sensed. To that end, consider a box containing a massless rod with two masses attached at its ends as presented in Figure 2. The rod is suspended by a torsion spring to allow in-plane rotation only. The spring is anchored to the box. At some moment when angular acceleration is applied to the box, a torque is generated. The torque is then balanced and sensed to obtain the angular acceleration. The sensing mechanism depends on the technology implemented in the angular accelerometer sensor.

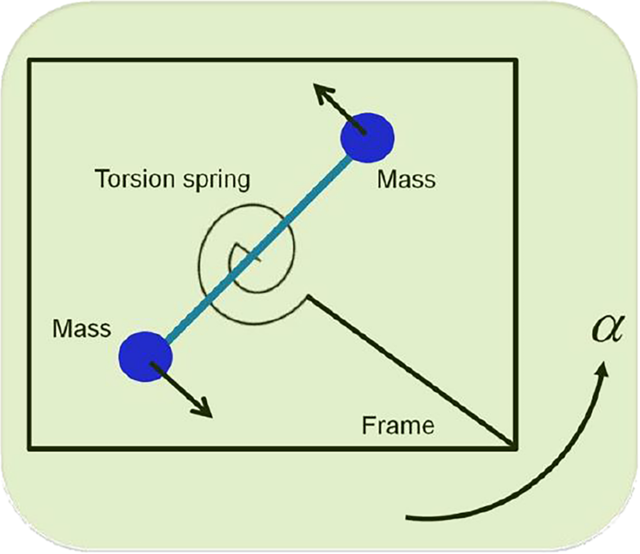

FIGURE 2 Principle of operation of angular accelerometer [Color figure can be viewed at wileyonlinelibrary.com and www.ion.org]

There are five common types of technologies upon which an angular accelerometer is based.

a. Fluid rotor angular accelerometers.[28]
b. Microfluidic channel angular accelerometers.[29]
c. Amorphous wire angular accelerometers.[30]
d. Piezoelectric angular accelerometers.[31-33]
e. MEMS angular accelerometers.[34-36]

The following is a description of the physical principles on which each accelerometer operates.

3.1 | Fluid rotor angular accelerometers

In fluid rotor accelerometers (Figure 3), a fluid mass is disposed in a passageway (a).[37] A paddle (b) is placed in that fluid for measuring forces applied to the paddle by the fluid mass as the fluid mass is accelerated. The sensor has a cylindrical geometry, and the paddle is pivoted into its base (c). When the accelerometer is placed in an environment in which it is to measure angular acceleration about its sensitive axis (d), a positive error signal is generated by the accelerometer as the fluid rotor (due to its inertia) tends to lag behind the accelerating case of the instrument. The paddle, which is disposed in the fluid path, constrains the fluid rotor to move with the case of the accelerometer. When acceleration occurs, the fluid rotor presses and shifts the paddle from its initial location. This paddle position change is sensed by a pickoff coil. This in turn serves as an error signal for a servo electromechanical control system[38] that restores the paddle to its zero position, preventing the fluid rotor from

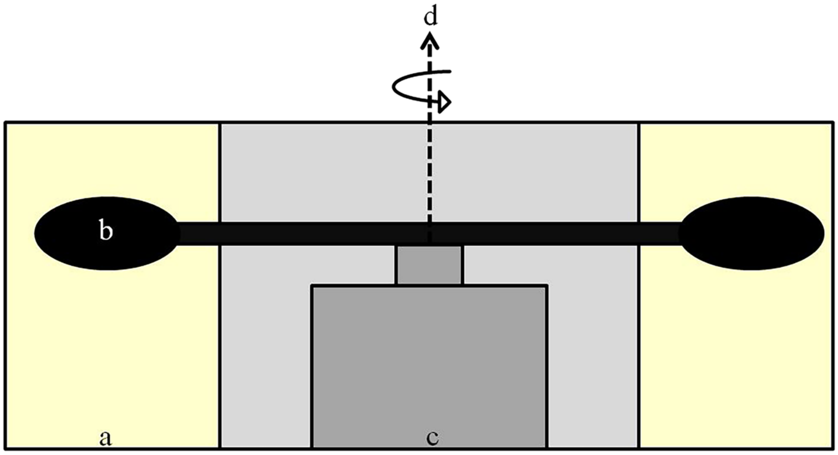

FIGURE 3 A fluid rotor accelerometer [Color figure can be viewed at wileyonlinelibrary.com and www.ion.org]

shifting in position and causing the fluid rotor to move with the case of the accelerometer. Thus, the electrical current generated by the servomechanism is proportional to the acceleration acting upon the fluid rotor.

3.2 | Microfluidic channel angular accelerometers

The microfluidic channel angular accelerometers (MFCAA; Figure 4) utilize fluid inertia to measure angular acceleration. When fluids undergo acceleration, the pressure inside them varies. This effect is used by the MFCAA to provide a measure of angular acceleration. A fluid-filled toroidal (a) serves as the sensing mechanism and contains a blockage (b) inside it, preventing any flow inside. Had there been no blockage located inside the tube, acceleration of the sensor case would generate a flow. Instead, in presence of the blockage, any angular acceleration will cause the inertia of the fluid to generate a pressure. Specific details regarding the traveling shockwaves inside the tube can be found at Wolfaardt and Heyns.[29] Eventually, the pressure waves will damp out due to various mechanisms, and steady-state differential pressure at the blockage will be observed. This differential pressure is proportional to the applied acceleration. In turn, any strain of the diaphragm blockage is detected and translated into an angular acceleration measurement.

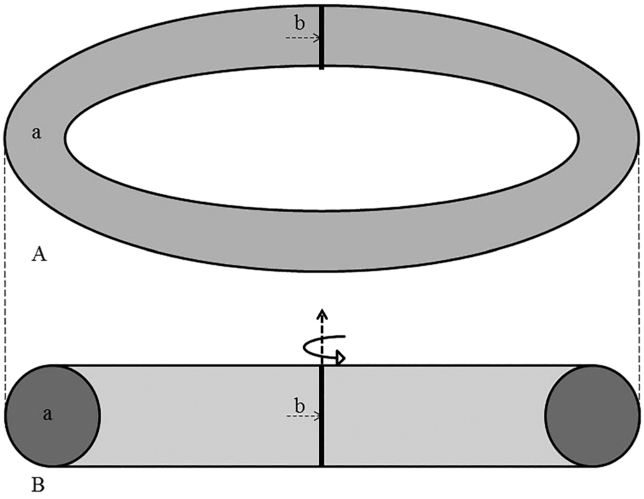

FIGURE 4 Microfluidic channel angular accelerometer. (A) Top view and (B) front section view

3.3 | Amorphous wire angular accelerometers

Amorphous wires-based accelerometers (Figure 5) utilize the Matteucci effect.[39] In brief, this is a phenomenon in which pulse voltage appears across the ends of a torsioned rod magnetized with an AC field applied parallel to its axis. The Matteucci effect is particularly attractive since it implements a transduction of magnetic to electrical signal without the requirement of pickup coils that are traditionally used in motion-sensing mechanisms to transform motion into an electric signal. In amorphous

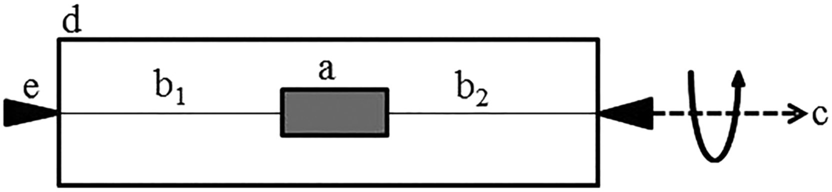

FIGURE 5 Amorphous wire angular accelerometer

wire accelerometers, a cylindrical seismic mass (a) is attached to two tensed amorphous wires (b_1 and b_2) in its center of mass. These wires are parallel to the mass symmetry axis (c) and fixed to the sensor housing (d). When the sensor undergoes acceleration, the seismic mass will be subjected to inertia forces. This in turn twists the wires causing a change in their magnetic properties, which triggers the Matteucci signal across the wire. The induced voltage, which is proportional to the applied angular acceleration,[30,40] is then sensed by the housing terminals (e).

3.4 | Piezoelectric angular accelerometers

The piezoelectric effect relates mechanical strain with electric current.[41] When piezoelectric material vibrates, it produces an electric signal proportional to its vibrational pattern input. A bimorph (Figure 6) is formed from two piezoelectric plates (a_1 and a_2) that are inversely polarized, then sandwiched, fused together, and connected to a rectangular beam (b).[42] The piezoelectric element of a bimorph serves as a seismic mass since it is mounted in a manner showing flexure when exposed to acceleration. The typical bimorph piezoelectric accelerometer is symmetric about a central fulcrum, with inverse polarized piezoelectric plates (c). During motion (Figure 7), linear acceleration (d) creates similar bending on both sides of the fulcrum, thus generating equal magnitude, but inverted, charges from each of the symmetric beams and therefore a self-cancelation occurs. Central rotations (e) flex the symmetric halves in opposite directions therefore the charges sum to provide an output proportional to angular acceleration about the fulcrum.

3.5 | MEMS angular accelerometers

MEMS-based devices usually utilize a vibrating proof mass that responds to motion in specific directions while attenuating others. Angular MEMS accelerometers (Figure 8) use this principle as well.[43] A proof mass (a) is attached to a cover plate (b) at a single anchor (c) using flexural springs. The anchor is at the center of the mass. While the mass is movable, it is constrained to rotate along its z axis that is perpendicular to it. When the mass is subjected to angular acceleration about its sensitivity axis, it rotates about its anchor point. The rotation of the proof mass is sensed capacitively. The edge of the moving mass has a comb-drive (d) structure and is used as serial capacitors with moving electrodes extending from it as

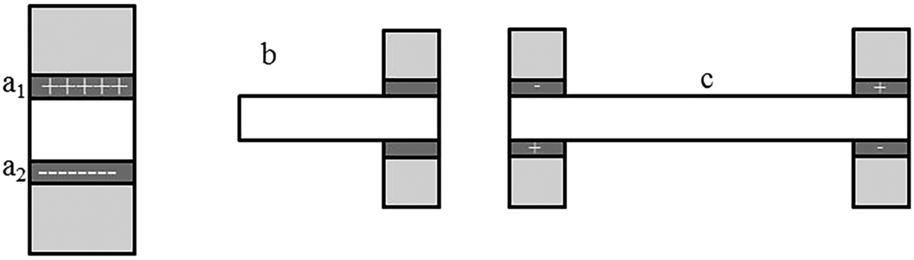

FIGURE 6 Piezoelectric angular accelerometer structure

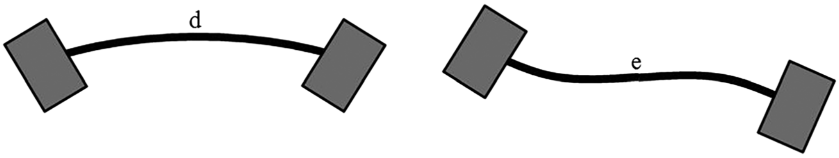

FIGURE 7 Piezoelectric angular accelerometer during motion

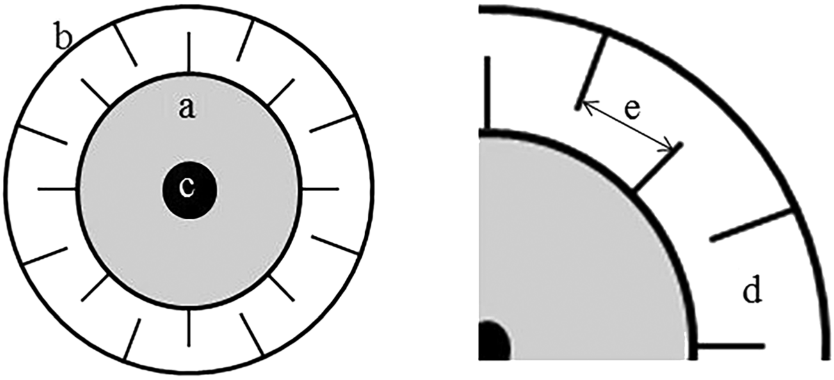

FIGURE 8 MEMS angular accelerometers

explained in Nasiri, Seeger, Taheri, and Yaralioglu.[36] During rotation, the distance between the electrodes (e) changes, causing a voltage increase over one of these capacitors, whereas the voltage over the other decreases. This voltage changes serves as the sensor output, and they are linearly proportional to the device angular acceleration.

4 | ANGULAR ACCELEROMETER-BASED INS

We propose two architectures for angular accelerometer-based INS, as presented in Figure 9. The first one, angular accelerometer INS (AINS), consists of linear and angular accelerometers whose outputs are specific force and angular acceleration vectors and thereby, after integration of the angular acceleration, is capable of functioning as a typical INS. In the second architecture, angular accelerometer-aided INS (AAINS), three orthogonal angular accelerometer sensors are augmented in the TINS architecture. In that manner, the system consists of nine sensors.

4.1 | AINS

In AINS, the IMU consists of linear and angular accelerometers that output specific force and angular acceleration vectors. The angular acceleration is integrated to obtain the angular rate that is used by the navigation processor to maintain the AINS attitude solution. The attitude solution is used to transform the specific force vector into the navigation frame. A gravity model is then used to obtain the acceleration from the specific force. Integrating the acceleration produces the velocity solution, and integrating the velocity yields the position solution. This procedure is illustrated in Figure 10.

For the derivation of the equations of motion, recall that angular velocity is required in TINS Equation (1),

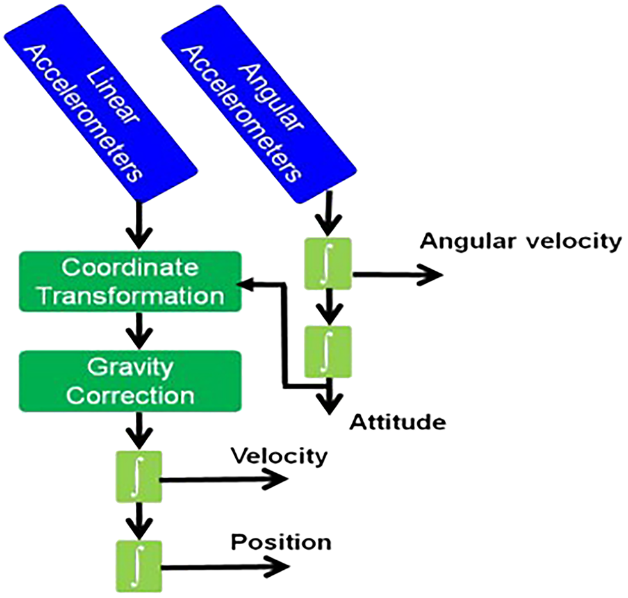

FIGURE 10 AINS block diagram [Color figure can be viewed at wileyonlinelibrary.com and www.ion.org]

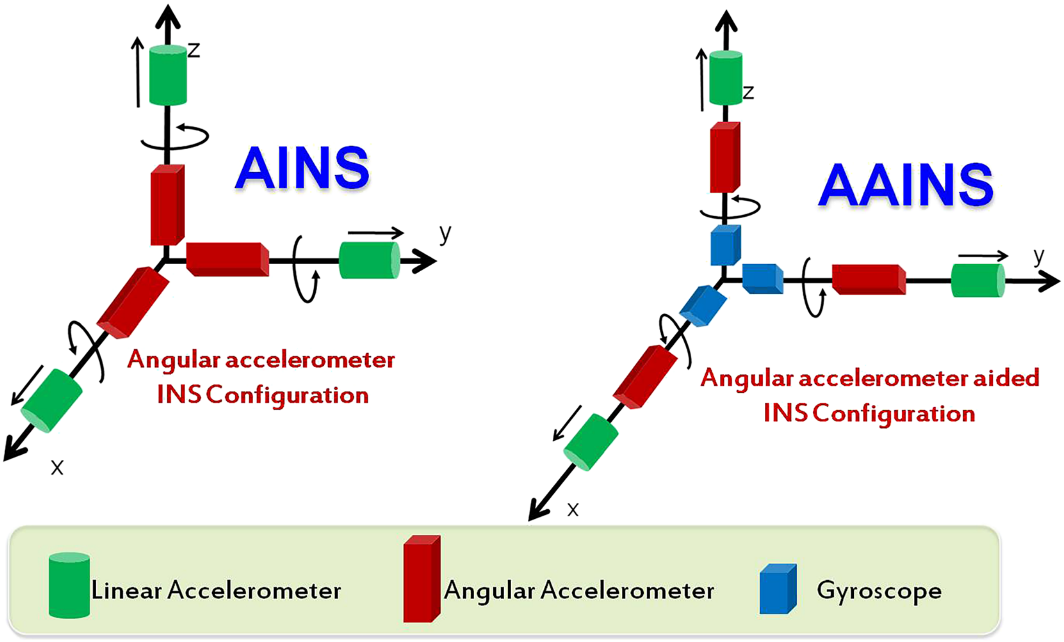

FIGURE 9 Suggested INS configurations [Color figure can be viewed at wileyonlinelibrary.com and www.ion.org]

therefore integration is performed on the measured angular acceleration.

$$\dot{\omega}_{ib}^{b} = \alpha_{ib}^{b}, \tag{8}$$

where α_{ib}^{b} is the angular acceleration between the body and inertial frames expressed in the body frame. The resultant equations of motion of AAINS are obtained by substituting (8) into (1).

$$\begin{aligned} \dot{p}_{LLH} &= \left[\frac{v_n}{R_M + h} + \frac{v_d}{(R_N + h)\cos\phi} - v_d\right]^T \\ \dot{v}_{eb}^{n} &= \dot{T}_b^n f_{ib}^{b} + g_{ib}^{n} - \left(\Omega_{en}^{n} + 2\Omega_{ie}^{n}\right) v_{eb}^{n} \\ \dot{T}_b^n &= T_b^n \Omega_{ib}^{b} - \left(\Omega_{ie}^{n} + \Omega_{en}^{n}\right) T_b^n \\ \dot{\omega}_{ib}^{b} &= \alpha_{ib}^{b} \end{aligned} \quad . \tag{9}$$

Thus the AINS has three more states, as in the GFINS configuration. In that manner, an additional integration is required to calculate the position, velocity, and attitude of the system. This integration is performed on the measured angular acceleration and therefore error terms (bias, scale factor, etc.) propagate into the calculations, degrading the navigation solution accuracy. On the other hand, high-frequency signals often related to measurement noise are filtered out as a result of the integration process.

Next, we define the following error-state vector:

$$\delta x = \left[\delta p^{n}\ \delta v^{n}\ \varepsilon^{n}\ \delta\omega^{b}\ b_a\ b_\alpha\right]^T, \tag{10}$$

where δp^{n},δv^{n} are the position and velocity errors; ε^{n} and $\delta\omega^{b}$ are the misalignment error and the angular velocity error, respectively; and finally, b_a and b_α are the accelerometers and angular accelerometers bias, respectively. Analyzing this model behavior will help us gain understanding regarding the influence of measurement errors on the AINS. To finalize, we define w_a and w_α as the accelerometer and angular accelerometer measurements noise and w_{ab},$w_{\alpha b}$ as the accelerometer and angular accelerometer bias. This yields the following error model:

$$\begin{bmatrix} \delta\dot{p}^{n} \\ \delta\dot{v}^{n} \\ \varepsilon^{n} \\ \delta\dot{\omega}^{b} \\ \dot{b}_a \\ \dot{b}_\alpha \end{bmatrix} = \begin{bmatrix} F_{rr} & F_{rv} & 0_{3\times3} & 0_{3\times3} & 0_{3\times3} & 0_{3\times3} \\ F_{vr} & F_{vv} & F_{v\varepsilon} & 0_{3\times3} & T_b^n & 0_{3\times3} \\ F_{\varepsilon r} & F_{\varepsilon v} & F_{\varepsilon\varepsilon} & T_b^n & 0_{3\times3} & 0_{3\times3} \\ 0_{3\times3} & 0_{3\times3} & 0_{3\times3} & 0_{3\times3} & 0_{3\times3} & I_3 \\ 0_{3\times3} & 0_{3\times3} & 0_{3\times3} & 0_{3\times3} & 0_{3\times3} & 0_{3\times3} \\ 0_{3\times3} & 0_{3\times3} & 0_{3\times3} & 0_{3\times3} & 0_{3\times3} & 0_{3\times3} \end{bmatrix} \begin{bmatrix} \delta p^{n} \\ \delta v^{n} \\ \varepsilon^{n} \\ \delta\omega^{b} \\ b_a \\ b_\alpha \end{bmatrix} + \begin{bmatrix} 0_{3\times3} & 0_{3\times3} & 0_{3\times3} & 0_{3\times3} \\ T_b^n & 0_{3\times3} & 0_{3\times3} & 0_{3\times3} \\ 0_{3\times3} & 0_{3\times3} & 0_{3\times3} & 0_{3\times3} \\ 0_{3\times3} & T_b^n & 0_{3\times3} & 0_{3\times3} \\ 0_{3\times3} & 0_{3\times3} & I_3 & 0_{3\times3} \\ 0_{3\times3} & 0_{3\times3} & 0_{3\times3} & I_3 \end{bmatrix} \begin{bmatrix} w_a \\ w_\alpha \\ w_{ab} \\ w_{\alpha b} \end{bmatrix}. \tag{11}$$

Full derivation of the dynamics matrix values can be found at Farrell.[4] Notice that the sensor error is modeled as an additive bias and white noise.

The explicit model is

$$\dot{b}_i = w_i, \tag{12}$$

where i is the sensor index.

4.2 | AAINS

The AAINS has the same TINS architecture with an additional three orthogonal angular accelerometers. However, the inertial sensors are used in a different way. The linear and angular accelerometers form the AAINS inertial measurement unit, and the gyroscope measurements are used as external measurements to aid the AAINS. In that manner, the AAINS architecture has the same equations of motion as the AINS architecture (9) and consequently has the same error model (10).

The gyroscope measurements are linear with the error-state vector but in order to apply such measurements, a nonlinear estimation approach must be implemented since the equations of motion (9) are nonlinear. In inertial navigation, usually an extended Kalman filter is employed with an error-state implementation,[3,4] yet other nonlinear estimation approaches exist. For example, unscented Kalman filter, eg, Walsh et al,[44] or state dependent Riccati equation filter, eg, Nemra and Aouf,[45] are both used for GPS/INS fusion.

Regardless of the nonlinear filter employed, the angular velocity is measured by the gyroscopes and thereby the angular velocity residual, which is part of the AAINS error-state model, is used as measurement. The measurement residual and matrix are defined by

$$\begin{aligned} \delta z_{\text{gyro}} &= \omega_{\text{AAINS}} - \omega_{\text{gyro}} \\ H_{\text{gyro}} &= \left[0_{3\times3} 0_{3\times3} 0_{3\times3} I_3 0_{3\times3} 0_{3\times3}\right]. \end{aligned} \tag{13}$$

A top-level block diagram of the AAINS architecture is illustrated in Figure 11. The AINS configuration is implemented to produce the navigation solution, namely, the position, velocity, and orientation. Gyroscope angular velocity measurements (13) are used as external measurements in a nonlinear filter with an error-state framework. The estimated error states are feed back to the AINS to correct both the navigation solution and inertial sensor error.

It is expected that with the angular velocity measurement, at least, the biases of the angular accelerometer will be estimated and removed during the calculation of the navigation solution process and thereby improvement in the AINS navigation solution accuracy will be achieved. This claim is verified in the following section.

5 | AINS ANALYTICAL ASSESSMENT

In this, section we provide an analytical assessment to the two AINS architectures for pure inertial navigation performance for short time periods. Yet, recall that the AAINS requires external sensor fusion of gyroscopes. Without the fusion process, both AINS architectures are identical and therefore the analytical evaluation provided in the first part of this section holds for both. In the second part, we provide an analytical observability analysis for the AAINS architecture during stationary conditions.

5.1 | Short-term navigation

As with most low-cost inertial systems, AINS is most suitable for short-term navigation (up to 8 min). When employing the standard assumptions of constant height and velocity (as in Titterton and Weston and Farrell[2,4]) in addition to the assumption that the Schuler term can be omitted for short-term navigation,[21] the resultant model for TINS north channel navigation degrades into[2]

$$\begin{aligned}
\delta\dot{x}_N &= \delta v_N \\
\delta\dot{v}_N &= g\varepsilon_E + b_{a,N} \\
\dot{\varepsilon}_E &= \omega_{ie}\cos(\phi)\delta\varepsilon_D + b_{g,E} \\
\dot{\varepsilon}_D &= b_{g,D}
\end{aligned}, \tag{14}$$

as illustrated in Figure 12.

Applying the same assumptions to the AINS model yields the following north channel equations:

$$\begin{aligned}
\delta\dot{x}_N &= \delta v_N \\
\delta\dot{v}_N &= g\varepsilon_E + b_{a,N} \\
\dot{\varepsilon}_E &= \omega_{ie}\cos(\phi)\delta\varepsilon_D + \delta\omega_E \\
\dot{\varepsilon}_D &= \delta\omega_D \\
\delta\dot{\omega}_E &= b_{\alpha,E} \\
\delta\dot{\omega}_D &= b_{\alpha,D} \\
\dot{b}_{a,N} &= 0 \\
\dot{b}_{\alpha,E} &= 0 \\
\dot{b}_{\alpha,D} &= 0
\end{aligned}, \tag{15}$$

where the subscripts N, E, and D indicate the navigation frame directions north, east, and down, respectively. This model is presented by the block diagram in Figure 13.

Notice that both (14) and (15) are linear and time invariant (LTI) systems and therefore can be solved analytically. A list of error sources and their influence on the positioning error in TINS (as previously derived in Titterton and Weston[2]), GFINS (as previously derived in Titterton and Weston[2]), and AINS is given in Table 1. As can be observed from the table, the initial position, velocity, and attitude errors cause the same position error for all three architectures. The initial linear accelerometer error also has the same influence on the position error. The position error arising from the gyro bias terms in the TINS configuration is analytically equivalent to that of the initial angular velocity of the AINS configuration.

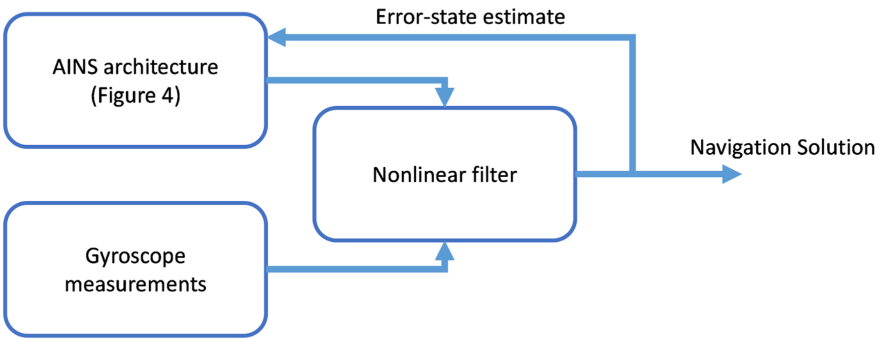

FIGURE 11 Top-level block diagram of AAINS architecture [Color figure can be viewed at wileyonlinelibrary.com and www.ion.org]

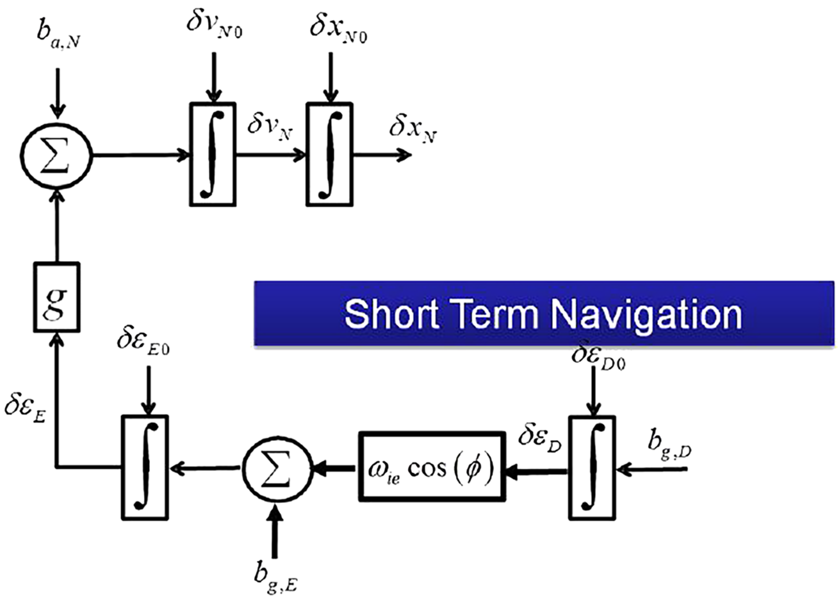

FIGURE 12 Short-term TINS north channel block diagram [Color figure can be viewed at wileyonlinelibrary.com and www.ion.org]

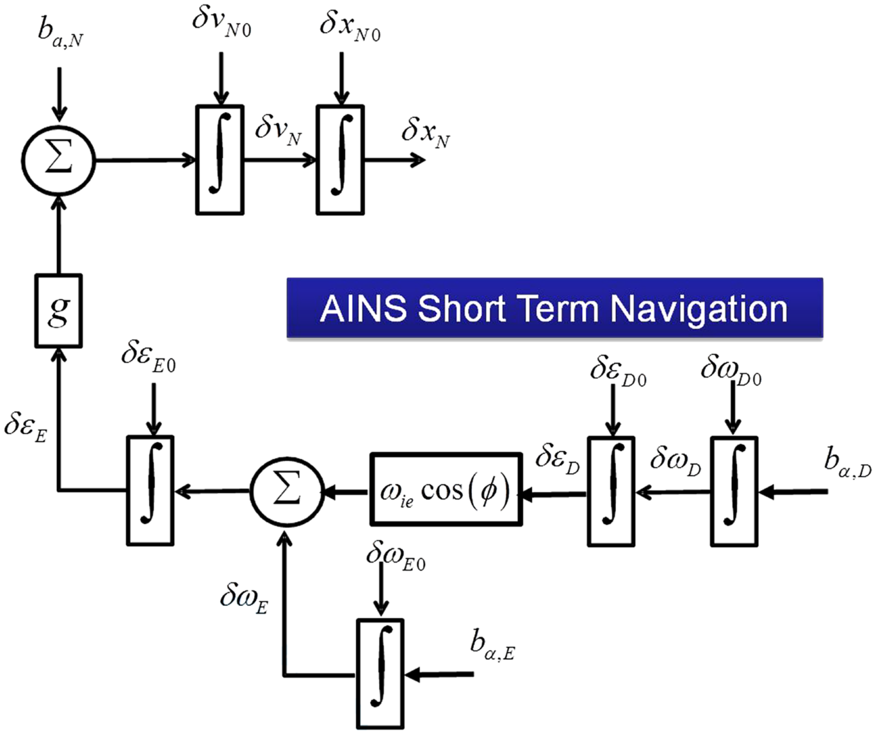

FIGURE 13 AINS short-term TINS north channel block diagram [Color figure can be viewed at wileyonlinelibrary.com and www.ion.org]

The only difference in the position error is due to the initial angular acceleration biases in the AINS configuration, which of course do not exist in the TINS configuration. The most dominant term in the position error in the AINS configuration is the angular accelerometer bias that is multiplied by the time to the power of four, while in the TINS, it is the gyro bias multiplied by the time to the power of three. The GFINS linear accelerometer bias is also multiplied by the time to the power of four, but it is also a function of the GF configuration used. Thus, for short time periods, only current sensor technology will determine which of the three will yield lower position error for pure inertial navigation.

5.2 | Simulation results

The error terms influence on the position error for short-term pure inertial navigation derived in Table 1 is evaluated. Since the initial position, velocity, and attitude terms are identical for the three architectures, they are not addressed in this example. In addition, if stationary

TABLE 1 Error terms influence on position error for short-term pure inertial navigation for three inertial navigation architectures

Error Source		TINS Position Error[2]	GFINS Position Error[22]	AINS Position Error
Initial position error	δx_{N0}	δx_{N0}	δx_{N0}	δx_{N0}
Initial velocity error	δv_{N0}	$t\delta v_{N0}$	$t\delta v_{N0}$	$t\delta v_{N0}$
Initial attitude error	$\delta \varepsilon_{D0}$	$g\frac{t^2}{2}\delta\varepsilon_{D0}$	$g\frac{t^2}{2}\delta\varepsilon_{D0}$	$g\frac{t^2}{2}\delta\varepsilon_{D0}$
Initial attitude error	$\delta \varepsilon_{E0}$	$\omega_{ie}c(\phi)g\frac{t^3}{6}\delta\varepsilon_{E0}$	N/A	$\omega_{ie}c(\phi)g\frac{t^3}{6}\delta\varepsilon_{E0}$
Initial angular velocity error	$\delta\omega_{D0}$	0	N/A	$\omega_{ie}c(\phi)g\frac{t^4}{24}\delta\omega_{D0}$
Initial angular velocity error	$\delta\omega_{E0}$	0	$g\frac{t^3}{6}\delta\omega_{E0}$	$g\frac{t^3}{6}\delta\omega_{E0}$
Gyro bias	δB_{gE}	$g\frac{t^3}{6}\delta B_{gE}$	0	0
Gyro bias	δB_{gD}	$\omega_{ie}c(\phi)g\frac{t^4}{24}\delta B_{gD}$	0	0
Accelerometer bias	δB_{aN}	$\frac{t^2}{2}\delta B_{aN}$	$g\frac{t^4}{24}e_2H_{\dot{\omega}}B_i\delta B_a + \frac{t^2}{2}e_1H_aB_i\delta B_a$	$\frac{t^2}{2}\delta B_{aN}$
Angular accelerometer bias	$\delta B_{\alpha E}$	0	0	$g\frac{t^4}{24}\delta B_{\alpha E}$
Angular accelerometer bias	$\delta B_{\alpha D}$	0	0	$\omega_{ie}c(\phi)g\frac{t^5}{120}\delta B_{\alpha D}$

conditions apply, the initial angular velocity errors are nullified. For the comparison, we chose a 12 accelerometer GF configuration composed of four triads—one in the center and the other three with an equal distance from the center and with the same orientation. As shown in Ovaska and Väliviita,[22] when assuming the body and navigation frame coincides, the influence of the linear accelerometer bias on the position error is given in (16), together with the corresponding TINS and AINS error terms from Table 1.

$$\begin{aligned}\delta P_{\text{TINS}} &= \frac{1}{2}t^2\delta B_{aN} + \frac{1}{6}gt^3\delta B_{gE}\\ \delta P_{\text{AINS}} &= \frac{1}{2}t^2\delta B_{aN} + \frac{1}{24}gt^4\delta B_{\alpha E}\\ \delta P_{\text{GFINS}} &= \frac{1}{8}t^2\delta B_{aN} + \frac{1}{96}gt^4\delta B_{aN}.\end{aligned} \tag{16}$$

Figure 14 illustrates the position error of the three inertial navigation architectures as given in (16) using a linear accelerometer bias of 5 mg, gyro bias of 10°/h, and angular accelerometer biases of 50, 5, and 0.5 mrad/s^2 (marked as red dashed lines). Results show that after 2 s, the TINS produced the lowest position error. At the end of the simulation time, only the AINS with bias value of 0.5 mrad/s^2 has the same order of error while the other two bias values of the AINS with the GFINS position error diverge rapidly. Up to 1 s, all architecture position errors have the same order of magnitude. This result is significant since usually GPS position updates are available at least at 1 Hz, bounding the growth of the position error.

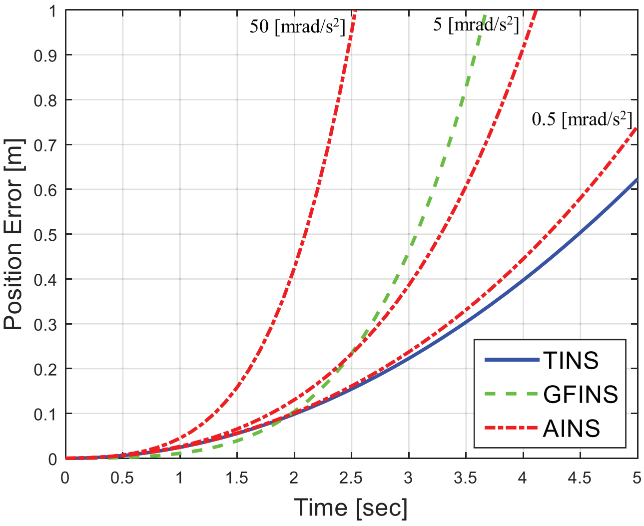

FIGURE 14 Comparison between TINS, GFINS, and AINS position error for pure inertial navigation for short time periods [Color figure can be viewed at wileyonlinelibrary.com and www.ion.org]

5.3 | Observability analysis AAINS

Loosely speaking, observability analysis is defined as a process for determining whether the state vector can be inferred from the measurements. The answer to a standard observability test of a given system and external measurement is binary, ie, yes or no. The question of which states (or some combination of them) are observable and which are not is of great importance. In particular, we address the AAINS architecture with the given system dynamics matrix defined in (11), angular velocity measurements matrix H_{gyro} defined in (13), and analytically derive the observable subspace. To that end, for stationary conditions, the observability matrix[4] is calculated

$$O = \begin{bmatrix} H_{\text{gyro}} \\ H_{\text{gyro}}F_{\text{AINS}} \\ \vdots \\ H_{\text{gyro}}F_{\text{AINS}}^{n-1} \end{bmatrix}, \tag{17}$$

where n is the dimension of the system. Evaluating (17) reveals that the rank of the observability matrix is six, that is, the system, as expected, is not completely observable. To find out which error states are observable, we follow the same procedure as in Klein.[21] A state transformation matrix is constructed using the image space of the observability matrix Im(O) and its null space null(O). The resultant transformation matrix is

$$T = [\mathrm{Im}(O)\mathrm{null}(O)]^T, \tag{18}$$

and the resulting observable subspace is

$$\mathrm{obs} = T\delta x = \left[\delta\omega^b b_\alpha\right]^T \in \mathbb{R}^6. \tag{19}$$

Equation (19) shows that the angular velocity error states are observable, which is expected since angular velocity measurements are employed. In addition, notice that the angular accelerometer biases are also observable using the gyro measurements, meaning that the AAINS architecture is inertly capable of estimating and removing the angular accelerometer bias and thereby improving the navigation accuracy.

6 | CONCLUSION

In this paper, angular accelerometers are utilized as a part of an INS. Two AINS architectures were proposed, and their associated equations of motion were derived. In the first configuration, the traditional gyroscopes were replaced by angular accelerometers while in the second configuration, gyroscopes serve as external aiding to the first architecture. For AINS navigation, an additional integration is required. As a result, sensor errors propagate rapidly into the navigation solution. Nevertheless, direct measurement of angular acceleration is preferred over its estimation for highly maneuvering platforms. Also, AINS architecture gives another option for the navigation engineer to pick an appropriate architecture for the task ahead.

An analytical derivation of the position error for short time periods of pure inertial navigation shows that up to a period of 1 s, all three architectures have the same performance when considering low-cost sensors. In addition, observability analysis for the AAINS architecture was performed to show that the angular accelerometer biases are observable during angular velocity updates.

Future research will include fusion between AINS and global positioning satellite systems to enable long navigation while maintaining highly dynamic performance.

ORCID

Uriel Nusbaum https://orcid.org/0000-0001-6701-8801

REFERENCES

1. Broxmeyer C. *Inertial Navigation Systems*. Artech House; 1964, 31, 4, 735.
2. Titterton D, Weston J. *Strapdown Inertial Navigation Technology*. 17 IET; 2004.
3. Groves PD. *Principles of GNSS, Inertial, and Multisensor Integrated Navigation Systems*. 2nd edition [Book review]. Artech House; 2015:30(2).
4. Farrell BJA. *Aided Navigation: GPS with High Rate Sensors*. 1st ed. Architectural Forensics McGraw-Hill, Inc.; March; 2008.
5. Williams D, Hu W, Davidson JW, Hiser JD, Knight JC, Nguyen-Tuong A. Security through diversity: Leveraging virtual machine technology. *IEEE Secur Priv*. 2009;7(1):26-33.
6. Shchekoldin AI, Shevyakov AD, Dema NU, Kolyubin SA. Adaptive head movements tracking algorithms for AR interface controlled telepresence robot. *2017 22nd International Conference on Methods and Models in Automation and Robotics (MMAR 2017)*. 2017:728–733.
7. Faion F, Zea A, Noack B, Steinbring J, Hanebeck UD. Camera- and IMU-based pose tracking for augmented reality. *IEEE International Conference on Multisensor Fusion and Integration for Intelligent Systems* 2017:648–653.
8. Li P, Qin T, Hu B, Zhu F, and Shen S. Monocular visual-inertial state estimation for mobile augmented reality. *Proceedings of the 2017 IEEE International Symposium on Mixed Augmented Reality (ISMAR 2017)*. 2017:11–21.
9. Varghese A, Chandra MG, Kumar K. Dual quaternion based IMU and vision fusion framework for mobile augmented reality. *Proceedings of WISP 2015 - IEEE International Symposium on Intelligent Signal Processing*. 2015.
10. Samata S. Mapping applied linguistics: a guide for students and practitioners. *Int J Biling Educ Biling*. 2012;15(1):119-123.
11. Skog I, Nilsson JO, Handel P, Nehorai A. Inertial sensor arrays, maximum likelihood, and Cramér-Rao bound. *IEEE Trans Signal Process*. 2016;64(16):4218-4227.
12. Tazartes D. An historical perspective on inertial navigation systems. *Proceedings of the 1st IEEE International Symposium on Inertial Sensors and Systems (ISISS 2014)*. 2014:1–5.
13. Benser ET. Trends in inertial sensors and applications. *Proceedings of the IEEE 2015 Inertial Sensors and Systems (ISISS 2015)*. 2015:1–4.
14. Lawrence A. *Modern Inertial Technology*. 2012.
15. Chen J-H, Lee S-C, DeBra DB. Gyroscope free strapdown inertial measurement unit by six linear accelerometers. *J Guid Control Dyna*. 1994;17(2):286-290.
16. Ang WT, Khosla PK, Riviere CN. Design of all-accelerometer inertial measurement unit for tremor sensing in hand-held microsurgical instrument. *IEEE International Conference on Robotics and Automation (ICRA 2003)*. 2003;2:1781–1786.
17. Hanson R, Pachter M. Optimal gyro-free IMU geometry. *AIAA Guidance, Navigation, and Control Conference and Exhibit* 2005:15–18.
18. Liu C, Zhang S, Yu S, Yuan X, Liu S. Design and analysis of gyro-free inertial measurement units with different configurations. *Sens Actuators A, Phys*. 2014;214:175-186.

19. Zappa B, Legnani G, van den Bogert AJ, Adamini R. On the number and placement of accelerometers for angular velocity and acceleration determination. *Transaction of the American Society of Mechanical Engineers. J Dyn Sys, Meas, Control*. 2001; 123(3):552-553.
20. Nusbaum U, Klein I. Feature article: Control theoretic approach to gyro-free inertial navigation systems. *IEEE Aerosp Electron Syst Mag*. 2017;32(8):38-45.
21. Klein I. Analytic error assessment of gyro-free INS. *J Appl Geod*. 2015;9(1):49-62.
22. Ovaska SJ, Väliviita S. Angular acceleration measurement: A review. *IEEE Trans Inst Meas*. 1998;47(5):1211-1217.
23. Godler I, Akahane A, Ohnishi K, Yamashita T. A novel rotary acceleration sensor. *IEEE Control Syst*. 1995;15(1):56-60.
24. Zulkarnain N, Imaduddin F, Zamzuri H, Mazlan SA. Application of an active anti-roll bar system for enhancing vehicle ride and handling. *CHUSER 2012–2012 IEEE Colloquium on Humanities, Science and Engineering Research* 2012:260–265.
25. Krid M, Benamar F. Design and control of an active anti-roll system for a fast rover. *IEEE International Conference on Intelligent Robots and Systems* 2011:274–279.
26. Eddy DS, Sparks DR. Application of MEMS technology in automotive sensors and actuators. *Proceedings of the IEEE*. 1998;86 (8):1747-1755.
27. Devasia S, Eleftheriou E, Moheimani SOR. A survey of control issues in nanopositioning. *IEEE Trans Control Syst Technol*. 2007;15(5, Special Issue):802-823.
28. Morris HD, Buckingham JT. Fluid rotor angular accelerometer. US Patent 3520196. 1970.
29. Wolfaardt HJ, Heyns PS. Dynamic modeling of a novel microfluidic channel angular accelerometer. *J Vib Control*. 2008;14 (4):451-467.
30. Lassow R, Meydan T. An angular accelerometer using amorphous wire. *IEEE Trans Magn*. 1995;31(6):3179-3181.
31. Kistler Instrument Corporation. Piezoelectric rotational accelerometer. US Patent 6397677 B1. 2006.
32. Tomikawa Y, Okada S. Piezoelectric angular acceleration sensor. *2003 IEEE Symposium on Ultrasonics*. 2003.
33. Ostwald F. Angular acceleration sensor with piezoelectric element. US Patent 3590289. 1971.
34. Arms SW, Townsend CP. MEMS based angular accelerometer. US Patent 20030047002 A1. 2003.
35. Statham LD. Angular accelerometer. US Patent 6257062 B1. 1957.
36. Nasiri SS, Seeger J, Taheri B, Yaralioglu GG. Vertically integrated 3-axis mems angular accelerometer with integrated electronics. US Patent 7934423 B2. 2011.
37. Statham LD. Angular accelerometer. US Patent 2946225A. 1957.
38. Morris HD. Position detecting transducer. US Patent 3074279. 1963.
39. Manabe T, Kawamura H, Mohri K, Yamasaki J, Malmhäll R, Ogasawara I. Large Barkhausen effect and Matteucci effect in cold-drawn amorphous magnetostrictive wires. *IEEE Transl J Magn Jpn*. 1988;3(3):288-293.
40. Meydan T. Application of amorphous materials to sensors. *J Magn Magn Mater*. 1994;133(1–3):525-532.
41. Wang LP, Woolf RA, Wang Y, et al. Design, fabrication, and measurement of high-sensitivity piezoelectric microelectromechanical systems accelerometers. *J Microelectromech Syst*. 2003;12(4):433-439.
42. DeVoe DL, Pisano AP. Surface micromachined piezoelectric accelerometers (PiXLs). *J Microelectromech Syst*. 2001;10(2): 180-186.
43. Liu H, Pike WT. A micromachined angular-acceleration sensor for geophysical applications. *Appl Phys Lett*. 2016;109(17): 173506-1-173506-5.
44. Walsh RM, Tymianski M, Wallace MC, Bath AP, Bance ML, Rutka JA. The transmatoid partial labyrinthectomy approach to medial skull base lesions. *Revue de Laryngologie Otologie Rhinologie*. 2000;121(1):13-20.
45. Nemra A, Aouf N. Robust INS/GPS sensor fusion for UAV localization using SDRE nonlinear filtering. *IEEE Sensors J*. 2010;10(4):789-798.

How to cite this article: Nusbaum U, Rusnak I, Klein I. Angular accelerometer-based inertial navigation system. *NAVIGATION*. 2019;66: 681–693. https://doi.org/10.1002/navi.336